

Massive black hole formation in dense stellar environments: Enhanced X-ray detection rates in high velocity dispersion nuclear star clusters

VIVIENNE F. BALDASSARE,¹ NICHOLAS C. STONE,² ADI FOORD,³ ELENA GALLO,⁴ AND JEREMIAH P. OSTRIKER^{5,6}

¹*Department of Physics and Astronomy, Washington State University, Pullman, WA 99163, USA*

²*The Racah Institute of Physics, The Hebrew University of Jerusalem, Israel*

³*Kavli Institute for Particle Astrophysics and Cosmology, Stanford University, Stanford, CA 94305, USA*

⁴*Department of Astronomy, University of Michigan, Ann Arbor, MI 48109, USA*

⁵*Department of Astrophysical Sciences, Princeton University, Princeton, NJ 08544, USA*

⁶*Department of Astronomy, Columbia University, New York 10027, USA*

(Received)

ABSTRACT

We analyze *Chandra X-ray Observatory* imaging of 108 galaxies hosting nuclear star clusters (NSCs) to search for signatures of massive black holes (BHs). NSCs are extremely dense stellar environments with conditions that can theoretically facilitate massive BH formation. Recent work by Stone et al. (2017) finds that sufficiently dense NSCs should be unstable to the runaway growth of a stellar mass BH into a massive BH via tidal captures. Furthermore, there is a velocity dispersion threshold (40 km s^{-1}) above which NSCs should inevitably form a massive BH. To provide an observational test of these theories, we measure X-ray emission from NSCs and compare to the measured velocity dispersion and tidal capture runaway timescale. We find that NSCs above the 40 km s^{-1} threshold are X-ray detected at roughly twice the rate of those below (after accounting for contamination from X-ray binaries). These results are consistent with a scenario in which dense, high-velocity NSCs can form massive BHs, providing a formation pathway that does not rely on conditions found only at high redshift.

1. INTRODUCTION

Every galaxy with stellar mass above $\sim 10^{10} M_{\odot}$ seems to host a massive black hole (massive BH; $M_{\text{BH}} \gtrsim 10^5 M_{\odot}$) at its center (Kormendy & Ho 2013). It remains unclear when and how these massive BHs form, although some sort of exotic high-mass seed formation mechanism may be required by the existence of the brightest high-redshift quasars (Haiman & Loeb 2001; Volonteri 2010; Inayoshi et al. 2020). Formation channels for massive BH seeds can be divided into two categories: those that operate only at high redshift, and channels which continue to produce massive BH seeds throughout cosmic time.

High redshift formation channels include the deaths of Population III stars (Madau & Rees 2001; Whalen & Fryer 2012) and direct-collapse black holes (Loeb & Rasio 1994; Begelman et al. 2006; Mayer et al. 2010; Latif et al. 2013). Both require the low-metallicity con-

ditions found only in the early universe. Channels in the latter category tend to invoke a gravitational runaway process which requires a dense star cluster (Portegies Zwart & McMillan 2002; Portegies Zwart et al. 2004; Gürkan et al. 2004). Because they are dynamically driven, they can operate at any redshift. These channels are of particular interest for their promise in forming intermediate-mass BHs ($M_{\text{BH}} \approx 10^2 - 10^5 M_{\odot}$). Recent theoretical works have illustrated the promise of dense young star clusters for forming black holes in the pair instability mass gap from $\sim 50 - 100 M_{\odot}$ (Kremer et al. 2020; González et al. 2021).

Nuclear star clusters (NSCs) have emerged as a promising stellar environment for facilitating the formation and/or growth of intermediate-mass BHs. NSCs reside at the centers of most galaxies with stellar masses between $\sim 10^8 - 10^{10} M_{\odot}$ (Côté et al. 2006; Sánchez-Janssen et al. 2019; Hoyer et al. 2021). NSCs themselves typically have masses in the range of $\sim 10^5 - 10^7 M_{\odot}$ with effective radii of a few parsecs, making them the densest known stellar environments (Böker et al. 2002, 2004; Turner et al. 2012; Ferrarese et al. 2006a; Leigh

et al. 2012; Georgiev & Böker 2014; Pouliaxis et al. 2019).

There are two main proposed channels for the formation of NSCs: globular cluster infall due to dynamical friction (Tremaine et al. 1975; Lotz et al. 2001; Capuzzo-Dolcetta & Miocchi 2008; Agarwal & Milosavljević 2011; Gnedin et al. 2014) and in situ star formation (Walcher et al. 2006; Seth et al. 2006). In practice, there are likely contributions from both channels, as NSCs have been found to contain multiple stellar populations (Carson et al. 2015; Neumayer et al. 2020; Fahrion et al. 2021; Hannah et al. 2021). The relative contribution of each channel likely depends on galaxy mass and environment (Hoyer et al. 2021).

It was once proposed that NSCs may take the place of massive BHs as the central compact massive object in low-mass galaxies¹ and follow similar scaling relations with their host galaxies (Ferrarese et al. 2006b). However, NSCs and massive BHs have been found to co-exist in some systems (Seth et al. 2008; Antonini 2013; Nguyen et al. 2018, 2021), including our own Milky Way (Schödel et al. 2009; Antonini et al. 2012). The precise relationship between NSCs and massive BHs remains unclear. NSCs could form around a pre-existing BH (Antonini 2013), and/or could provide an environment in which massive BHs can more easily form.

Several dynamical processes have been proposed for the formation of an intermediate-mass BH within a NSC (Gürkan et al. 2004; Miller & Davies 2012; Stone et al. 2017; Antonini et al. 2019; Fragione & Silk 2020; Nataraajan 2021; Fragione et al. 2021). Miller & Davies (2012) suggest that massive BHs will form at any epoch in a NSC with a velocity dispersion greater than a critical value of $\sigma \approx 40 \text{ km s}^{-1}$. This is because above 40 km s^{-1} , heating from primordial binaries is unable to prevent the system from undergoing core collapse. Core collapse will produce a BH subcluster; interactions within the subcluster will then either leave one or no stellar-mass BHs. If there is no BH, one will form from runaway stellar mergers (Portegies Zwart & McMillan 2002). In both cases, the remaining stellar-mass BH proceeds to grow quickly through tidal capture and/or disruption events into a massive BH.

Stone et al. (2017) expands on the above works by calculating the circumstances necessary for a NSC to grow a central stellar-mass BH into a massive one. They specifically consider a runaway tidal capture pro-

cess. Tidal capture has the largest cross section for any dynamical interaction process in a dense star cluster (Fabian et al. 1975; Lee & Ostriker 1986). Once there is a stellar-mass BH left at the center of the NSC, it can grow into an intermediate-mass BH through runaway tidal capture, provided that the NSC has sufficiently high central density and velocity dispersion. The runaway tidal capture will slow once the BH reaches $\sim 10^{2-3} M_{\odot}$. At this point, BH growth will continue through tidal captures and disruptions (and possibly also standard accretion processes) until the BH reaches massive size. Stone et al. (2017) compute a timescale for this process called the tidal capture rate (TC rate, or \dot{N}_{TC}). They find that many existing NSCs have rates indicating they are unstable to this runaway growth. Stated another way, given a sufficiently dense NSC, tidal capture and tidal disruption will inevitably grow a stellar-mass BH into a massive BH in less than a Hubble time.

The theoretical works described above reach a general consensus that NSCs should be able to form massive BHs through dynamical processes if they have velocity dispersions greater than $\sim 40 \text{ km s}^{-1}$. Indeed, there is already tentative observational evidence for this point: dynamically confirmed massive BHs are very common in galaxies with $\sigma \gtrsim 40 \text{ km s}^{-1}$, and uncommon below this threshold (see e.g. Stone et al. 2017 Fig. 1 or Greene et al. 2020 Fig. 3). However, we emphasize here the circumstantial nature of existing evidence: dynamical mass measurements are challenging in the smallest galaxies, and the upper limits on BH mass produced by non-detections do not generally fall well below extrapolations of galaxy scaling relations (Greene et al. 2020, although there are notable exceptions to this, such as M33; Gebhardt et al. 2001).

Here, we adopt a completely different approach to explore the massive BH population amongst NSCs above and below the proposed 40 km s^{-1} threshold. Specifically, we use *Chandra X-ray Observatory* (CXO) imaging to search for X-ray emission in NSCs, as sufficiently bright X-ray emission is evidence for the presence of a massive BH. We then compare the velocity dispersions and TC rates of NSCs with/without X-ray emission. This approach provides a novel consistency check for the predictions of the TC runaway theory.

In Section 2, we describe the sample of NSCs. In Section 3, we describe the X-ray analysis and our assessment of X-ray binary contamination. Section 4 presents our results, and we discuss their implications in Section 5.

2. SAMPLE PROPERTIES

¹ The absence of NSCs from the most massive galaxies is likely due to the richer merger history of the largest systems, which suffer from “core scouring” following major and some minor mergers (Ebisuzaki et al. 1991; Quinlan 1996).

Object	RA [deg]	Dec [deg]	Dist. Modulus	Distance [Mpc]	\dot{N}_{TC} [yr ⁻¹]	Velocity Dispersion [km s ⁻¹]	Core Resolve
ESO138-G010	254.76196	-60.21606	30.84	14.72	1.71E-11	93.39	0
ESO241-G006	359.0625	-43.4275	31.44	19.41	1.12E-09	23.99	1
ESO359-G029	63.21058	-33.00333	30.03	10.14	2.66E-08	29.47	1
IC0239	39.11596	38.96903	30.76	14.19	4.96E-11	30.88	0
IC0396	74.495792	68.323383	30.79	14.39	9.79E-12	100.86	0
IC4710	277.15812	-66.98225	29.75	8.91	2.37E-08	67.15	1
IC5256	342.44071	-68.69072	33.52	50.58	1.84E-10	22.01	1
IC5332	353.6145	-36.10156	29.62	8.39	2.34E-11	10.43	0
M074	24.174	15.78333	29.93	9.68	1.44E-09	82.51	1
M108	167.87896	55.67414	30.6	13.18	5.57E-11	32.07	0
MCG-01-03-085	16.27033	-6.21242	30.28	11.38	1.29E-10	41.97	0
NGC0247	11.78567	-20.76044	27.81	3.65	1.36E-08	60.35	1
NGC0428	18.23175	0.98167	30.86	14.86	1.43E-09	79.84	0
NGC0672	26.97508	27.43219	29.44	7.73	3.23E-11	21.04	0
NGC0959	38.09971	35.49461	30.47	12.42	5.06E-12	25.49	0
NGC1003	39.81917	40.87275	30.16	10.76	5.77E-10	56.43	1
NGC1042	40.09996	-8.43364	29.56	8.17	1.12E-08	84.03	1
NGC1058	40.87546	37.34111	29.85	9.33	1.86E-08	238.72	1
NGC1073	40.9185	1.37583	30.7	13.80	1.28E-08	124.05	0
NGC1325A	51.20192	-21.33614	31.7	21.88	9.25E-10	50.19	1
NGC1385	54.36796	-24.50128	30.62	13.30	1.52E-07	107.57	1
...

Table 1. Sample of 108 galaxies with NSCs and CXO observations. Distance moduli are from [Georgiev et al. \(2016\)](#). Tidal capture rates (\dot{N}_{TC}) and velocity dispersions are computed in [Stone et al. \(2017\)](#). A full version of this table is available in the online version.

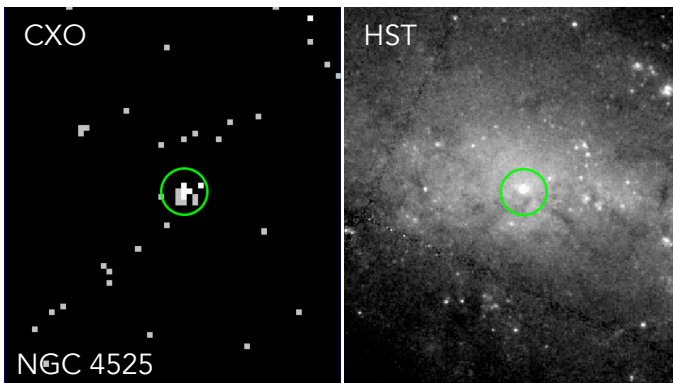


Figure 1. *Chandra X-ray Observatory* imaging (left) and *Hubble Space Telescope* imaging (right) for NGC 4525, a galaxy with a nuclear X-ray point source. The green circles have a radius of 2'' and are centered on the galaxy coordinates from [Georgiev & Böker \(2014\)](#). The HST image was taken with the WFPC2 in the F814W band. The NSC is visible in the HST image.

Our parent sample contains 207 nearby ($D < 50$ Mpc) galaxies hosting NSCs. All 207 have *Hubble Space Telescope* observations, which are necessary in order to resolve the scales necessary to study NSCs. These are se-

lected from the samples of [Böker et al. \(2004\)](#); [Côté et al. \(2006\)](#) and [Georgiev & Böker \(2014\)](#) and were compiled by [Stone et al. \(2017\)](#) in order to compute tidal capture runaway timescales for actual NSCs. The parent sample consists of NSCs in both late and early-type galaxies.

All NSCs in the sample were modeled by a King profile (a tidally truncated isothermal sphere; [King 1966](#)), and have measured total masses, effective (half-light) radii, and concentration parameters. Note that for modeling, the concentration parameter (defined as $C = r_{\text{tidal}}/r_{\text{core}}$) was restricted to the set of $\{5, 15, 30, 100\}$ due to computational limitations. The galaxy stellar masses and NSC stellar masses for the parent sample were computed by [Georgiev et al. \(2016\)](#).

CXO observations were available in the archive or newly acquired for 108 out of 207 galaxies (see Section 3). These 108 galaxies are the focus of our analysis. The 108 galaxies in our sample range in distance from 2 – 50 Mpc. Galaxy masses range from $10^8 - 10^{11} M_{\odot}$. The NSC masses range from $1 \times 10^5 - 2 \times 10^8 M_{\odot}$, and effective radii range from 0.3 – 42 pc. The sample of 108 objects is presented in Table 1.

3. X-RAY ANALYSIS

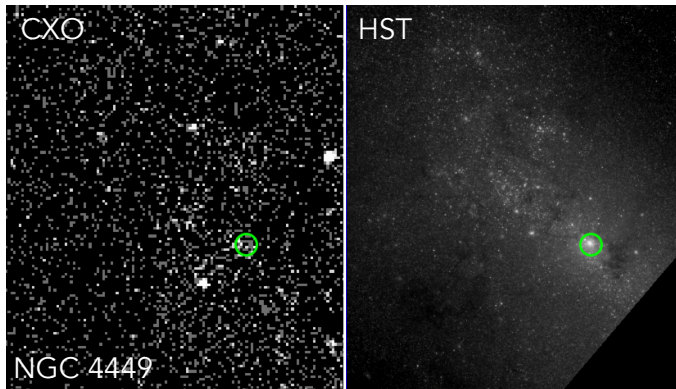


Figure 2. *Chandra X-ray Observatory* imaging (left) and *Hubble Space Telescope* imaging (right) for NGC 4449, a galaxy with diffuse X-ray emission in the center. The green circles have a radius of $2''$ and are centered on the galaxy coordinates from [Georgiev & Böker \(2014\)](#). The HST image was taken with the ACS WFC in the F814W band. The NSC is visible in the HST image.

We use CXO observations to study X-ray emission from our sample of NSCs. The angular resolution of CXO is necessary for determining whether any X-ray emission is coincident with the NSC. We searched the CXO archive for ACIS observations of the NSC sample. These were combined with our own program targeting the most dense, highest velocity dispersion NSCs. Fourteen objects were targeted with our program (GO 20700424; PI Baldassare), and 94 objects were in the CXO archive.

All observations were reprocessed and analyzed with the Chandra Interactive Analysis of Observations software (CIAO; version 5.13). We generate an initial source list using CIAO WAVDETECT. We then correct the astrometry by cross-matching the X-ray source list with sources in the USNO B-1 catalog. Matches were required to be within $2''$ of one another, and we required three or more matches to apply the astrometry correction. We next filtered out any background flares in the observations. We then applied an energy filter in the 0.5-7 keV range and reran WAVDETECT with a threshold significance of 10^{-6} , which corresponds to one false detection over a single ACIS chip.

Using SRCFLUX, we computed count rates, fluxes, and uncertainties in the soft (0.5-1.2 keV), broad (0.5-7 keV), and hard (2-10 keV) bands. We take the coordinates given by [Georgiev & Böker \(2014\)](#) to be the NSC position. If there was a WAVDETECT source coincident with the galaxy center, we extracted the counts in a circular region with a radius of $2''$ at the WAVDETECT source position. If there was not a source detected at the nucleus, we extracted counts in the same size circular region centered on the [Georgiev & Böker \(2014\)](#) coordi-

nates. For the background region, we use a source-free annulus with inner and outer radii of ~ 20 and ~ 35 arcseconds, respectively. We compute the unabsorbed model flux for a power law spectrum with $\Gamma = 1.8$ and the Galactic n_{H} value returned by the CIAO colden tool.

In all, 46/109 objects are X-ray detected. However, 5 of the 46 have diffuse X-ray emission rather than point sources. We do not consider these five as possible BHs and do not analyze them with the other 41 sources. An example of a galaxy with a nuclear X-ray point source is shown in Figure 1 and an example of a diffuse source is shown in Figure 2.

Of the 41 NSCs with X-ray point sources, 35 are detected in both the 0.5-7 and 2-10 keV bands, and 6 are only significantly detected in the 0.5-7 keV band. Luminosities in the 0.5-7 keV band range from $2.0 \times 10^{37} - 2.0 \times 10^{42} \text{ erg s}^{-1}$, with a median luminosity of $1.2 \times 10^{39} \text{ erg s}^{-1}$. The X-ray luminosities and upper limits are given in Table 2.

3.1. X-ray binary contamination

Given the X-ray luminosities found for the NSCs in our sample, we must consider the possibility of contamination from X-ray binaries. While it is difficult to state definitively whether any particular source is a massive BH or an X-ray binary, we can estimate the likely X-ray luminosity from low-mass X-ray binaries (LMXBs) and high-mass X-ray binaries (HMXBs) for each NSC. The contribution from LMXBs traces the cumulative star formation history of the galaxy, and is thus proportional to the total stellar mass ([Gilfanov 2004](#)). The contribution from HMXBs traces recent star formation in the galaxy, and is proportional to the galaxy’s star formation rate ([Grimm et al. 2003](#); [Mineo et al. 2012](#)).

[Lehmer et al. \(2019\)](#) uses a sample of 38 nearby galaxies to constrain the scaling relations for X-ray binaries. Their sample spans a wide range in galaxy morphology, stellar mass, star formation rate, and metallicity. It includes both nucleated and non-nucleated galaxies; several of the galaxies in their sample overlap with our sample of 108 galaxies. The expected X-ray luminosity from LMXBs and HMXBs is given by

$$L_{\text{X}} = \alpha M_{*} + \beta \text{SFR}. \quad (1)$$

The best fit values from [Lehmer et al. \(2019\)](#) are $\alpha = 1.8 \times 10^{29} \text{ erg s}^{-1} M_{\odot}^{-1}$ and $\beta = 5.1 \times 10^{39} \text{ erg s}^{-1} (M_{\odot} \text{ yr}^{-1})^{-1}$. We compute the expected X-ray binary luminosity for each of our galaxies. Note that this uses the 0.5-8 keV luminosity; we compute the 0.5-8 keV luminosities for our X-ray sources in order to compare to the estimated luminosities from [Lehmer et al. \(2019\)](#).

Galaxy stellar masses are taken from [Georgiev & Böker \(2014\)](#). To compute the SFRs, we use the formalism from [Kennicutt & Evans \(2012\)](#), where

$$\log \dot{M}_*(M_\odot \text{ yr}^{-1}) = \log L_{\text{FUV,corr}} - 43.35. \quad (2)$$

The FUV luminosity is corrected for dust extinction using the $25\mu\text{m}$ luminosity, where $L_{\text{FUV,corr}} = L_{\text{FUV,obs}} + 3.89 \times L_{25\mu\text{m}}$.

We use GALEX data ([Martin et al. 2005](#)) to measure the FUV luminosities for each galaxy in our sample. We measure the FUV flux within an aperture with a radius equal to the galaxy radius reported in [Georgiev & Böker \(2014\)](#) (their R_{25} , from HyperLeda; [Paturel et al. 2003](#)). We use W4 magnitudes from AllWISE ([Wright et al. 2010](#)) to compute the $25\mu\text{m}$ flux density and correct the FUV luminosity.

We are interested in the expected X-ray binary luminosity within the CXO point spread function. Following similar analyses presented in [Foord et al. \(2017\)](#) and [Lee et al. \(2019\)](#), we assume that the galaxy mass traces the light profile, and measure the fraction of galaxy light in the central $2''$ for each system using available HST imaging. We note that galaxies were imaged with different cameras and filters. The median fraction of light in the central $2''$ is 0.035. For a handful of cases, the galaxy is larger than the HST image field of view; for these galaxies, we take the fraction to be 0.05, slightly more conservative than the median value.

Putting the above steps together, we find expected X-ray binary luminosities in the central $2''$ ranging from $6 \times 10^{36} - 3 \times 10^{39} \text{erg s}^{-1}$. The ratio of observed 0.5-8 keV luminosity to that expected from X-ray binaries ranges from 0.09 to 3980, with a median ratio of 6.27. Table 3 gives the expected X-ray binary luminosities and ratios of observed-to-expected luminosity.

A caveat to this analysis is that it does not take into account additional potential emission due to the NSC environment, i.e., preferential LMXB/HMXB formation in the central parsecs. Additionally, a possible formation channel for NSCs is through inspirals of globular clusters, where X-ray binary formation is efficient ([Clark 1975](#); [Sivakoff et al. 2007](#)). As our formation channel is driven by runaway tidal capture LMXB formation in NSCs, this may seem contradictory. However, we consider as a comparison case the central pc of the Milky Way galaxy, which indeed possesses an overabundance of LMXBs ([Hailey et al. 2018](#)), that may themselves be BH-LMXBs that have formed through tidal capture ([Generozov et al. 2018](#)). Except during brief periods of LMXB outburst ([Muno et al. 2005](#)), the combined X-ray luminosity of this LMXB subcluster is $\lesssim 10^{34} \text{erg s}^{-1}$, likely due to the low mass-transfer

rates in most tidal capture LMXBs. Furthermore, the Milky Way NSC lacks clear evidence for an overabundance of NS-LMXBs, which form at elevated rates in globular clusters due to chaotic binary-single scatterings ([Ivanova et al. 2008](#)). This signifies (i) a low rate of NS-LMXB formation in NSCs relative to globular clusters, likely due to lower binary fractions resulting from the higher velocity dispersion environment of the galactic nucleus², and (ii) that whatever NS-LMXBs were brought in through globular inspiral have since deactivated. As the typical NS-LMXB lifetime is ~ 1 Gyr ([Ivanova et al. 2008](#)), the latter conclusion would be unsurprising if most globular inspiral events happened in the distant past.

Given the generally low X-ray luminosity of LMXBs in the Milky Way NSC and lacking a NSC-specific XRB luminosity estimator, we proceed with our estimates of probable X-ray emission based on SFR and stellar mass within the PSF. We note, however, that we may be under-predicting the true total XRB luminosity of some NSCs if their dynamics deviates strongly from that of the Milky Way NSC.

Going forward, we consider anything with an observed luminosity a factor of 2 higher than expected to be due to a massive BH (e.g., [Birchall et al. 2020](#)). Objects with observed luminosities less than twice the expected are treated as non-detections. This removes 10 detections from the $\sigma > 40 \text{km s}^{-1}$ regime, and 2 from the $\sigma < 40 \text{km s}^{-1}$ regime. These tend to be lower luminosity systems; the median 0.5-7 keV luminosity for the likely X-ray binary systems is $\sim 10^{38} \text{erg s}^{-1}$, compared to $10^{39} \text{erg s}^{-1}$ for the more secure massive BHs. Our results do not change if we use a more conservative factor of 3 instead of 2.

² However, the Milky Way NSC has a high velocity dispersion and low binary fraction at least in part because of the presence of a SMBH; in an NSC lacking a central massive BH, the binary fraction might be high enough to favor dynamical NS-LMXB formation in three-body scatterings.

Table 2. X-ray properties

Object	ObsID	Exp Time [ks]	$L_{0.5-7}$	$L_{0.5-7, \text{lower}}$	$L_{0.5-7, \text{upper}}$	L_{2-10}	$L_{2-10, \text{lower}}$	$L_{2-10, \text{upper}}$	Diffuse
ESO138-G010	14800	9.84	38.04	37.58	38.37	-	-	38.36	N
ESO241-G006	17004	4.7	-	-	38.32	-	-	38.71	N
ESO359-G029	21468	3.07	-	-	38.06	-	-	38.34	N
IC0239	7131	4.53	-	-	38.01	-	-	38.47	N
IC0396	7134	4.87	39.08	38.94	39.22	38.69	38.24	39.02	N
IC4710	9877	15.25	-	-	37.28	-	-	37.52	N
IC5256	17001	1.65	-	-	39.58	-	-	39.99	N
IC5332	2067	55.24	-	-	36.47	-	-	37.02	N
M074	4753	5.28	38.05	37.71	38.32	38.04	37.28	38.49	N
M108	2025	59.36	37.61	37.42	37.78	37.41	36.44	37.80	Y
MCG-01-03-085	12981	9.82	-	-	37.48	-	-	38.11	N
NGC0247	17547	5.01	39.19	39.16	39.22	39.17	39.12	39.22	N
NGC0428	16978	3.99	-	-	38.17	-	-	38.55	N
NGC0672	7090	2.15	-	-	40.90	-	-	41.46	N
NGC0959	7111	2.18	-	-	38.17	-	-	38.65	N
NGC1003	7116	2.67	-	-	38.03	-	-	38.50	N
NGC1042	12988	29.01	38.09	37.98	38.18	38.16	37.99	38.31	N
NGC1058	387	2.41	38.00	37.45	38.37	38.34	37.57	38.80	N
NGC1073	4686	5.74	38.90	38.75	39.03	39.03	38.80	39.22	N
NGC1325A	7841	5.09	-	-	38.28	-	-	38.76	N
NGC1385	21473	5.04	42.22	42.09	42.32	42.28	42.11	42.40	N
NGC1483	16981	2.51	-	-	39.01	-	-	39.37	N
NGC1487	21469	2.05	-	-	38.12	-	-	38.40	N
NGC1493	7145	10.03	38.76	38.64	38.85	38.47	38.18	38.70	N
...

NOTE—Columns 4-6 give the log of the 0.5-7 keV luminosity (in erg s^{-1}), lower limit, and upper limit, respectively. Columns 7-9 give the log of the 2-10 keV luminosity (in erg s^{-1}), lower limit, and upper limit, respectively. Column 10 states whether the detected X-ray emission was diffuse. The complete table is available in the online version of this paper.

In Figure 3, we show the X-ray luminosity versus galaxy mass, NSC mass, and star formation rate for likely massive BHs and likely XRBs. At a given X-ray luminosity, the likely XRBs tend to be in more massive galaxies and those with higher SFRs. This is expected as more massive galaxies will have more stellar mass within the central $2''$.

In addition to the 12 point source objects we treat as likely X-ray binaries, all five of the galaxies with diffuse X-ray emission have X-ray luminosities less than the expected luminosity from X-ray binaries. Their luminosities range from $\sim 0.1 - 0.5$ times the expected X-ray binary luminosity.

3.2. Hardness ratios

We compute hardness ratios for our sources using the aperture fluxes reported by SRCFLUX. The hardness ratio is given by $[F(H) - F(S)]/[F(H) + F(S)]$ where $F(H)$ is the flux in a hard band and $F(S)$ is the flux in a soft band. Here, we use the 0.5-2 keV band as the soft band and the 2-7 keV band as the hard band. In Figure 4, we show the hardness ratios for the likely active galactic nuclei (AGN) and likely XRBs. The samples of likely AGN and XRBs both span a wide range in hardness ratios (from -1 to 1), with similar distributions. Many are consistent with a typical AGN spectrum with $\Gamma = 1.8$.

4. RESULTS

As described in Section 3, 41 NSCs have X-ray point sources coincident with the NSC position. 12 of these have X-ray luminosities close to the expected values for X-ray binary emission based on the scaling relations derived by Lehmer et al. (2019). In this section, we explore the properties, velocities dispersions, and tidal capture rates of NSCs with/without X-ray emission, treating the 12 likely X-ray binary contaminants as non-detections. Henceforth, “X-ray detected” refers to galaxies with X-ray detections likely to be from a massive BH.

4.1. Galaxy properties

In Figure 5, we show the distributions of galaxy mass, NSC mass, and effective radius for galaxies with and without X-ray detected NSCs. This is important for understanding what factors influence a NSC hosting an X-ray active BH. The masses and effective radii were measured by Georgiev et al. (2016) based on multi-band HST imaging.

The median galaxy stellar masses for the X-ray detected and non-detected galaxies are $5.9 \times 10^9 M_\odot$ and $2.8 \times 10^9 M_\odot$, respectively. The X-ray detected NSCs tend towards slightly higher-mass galaxies. The me-

dian NSC stellar masses for the X-ray detected and non-detected galaxies are $3.5 \times 10^6 M_\odot$ and $2.3 \times 10^6 M_\odot$, respectively, and the distribution for X-ray detected NSCs skews towards slightly higher NSC masses. Finally, the median effective radii for the two samples are similar; 2.4 and 2.5 pc.

4.2. Detection rate versus velocity dispersion

Our goal in this section is to compare the X-ray properties of NSCs with velocity dispersions above and below the 40 km s^{-1} threshold. The cluster averaged velocity dispersion σ is defined by $\sigma = \sqrt{G M_{\text{tot}}/(3 r_{\text{eff}})}$ where r_{eff} is the half-mass radius from the best-fit King model. In Figure 6, we show the X-ray luminosity versus velocity dispersion for the entire sample.

However, we cannot take the detection fractions above and below this velocity dispersion threshold at face value. The X-ray sample is non-homogeneous and observations have different limiting fluxes. To account for this, we compute the fraction for samples with artificially imposed X-ray detection limits. For each imposed detection limit L_{det} , we exclude any non-detections with upper limits greater than that value (since we cannot say whether they are detected down to a limit of L_{det}). We count the number of NSCs with measured X-ray luminosities greater than L_{det} , and treat anything with an X-ray luminosity lower than L_{det} as a non-detection. Note that any galaxies with X-ray luminosities likely to be due to X-ray binaries are also treated as non-detections. We then compare the number of detected NSCs against those with upper-limits lower than L_{det} . We repeat this for different values of L_{det} . Figure 7 demonstrates how the sample looks for different values of L_{det} . Figure 8 shows X-ray detection fraction versus L_{det} for NSCs above and below the velocity dispersion threshold.

From Figures 7 and 8, we can see that for all values of L_{det} , the detection fraction is significantly higher for the $\sigma > 40 \text{ km s}^{-1}$ sample. At $L_{\text{det}} = 10^{39} \text{ erg s}^{-1}$, the detection fraction for $\sigma < 40 \text{ km s}^{-1}$ is $6_{-5}^{+8}\%$ and the detection fraction for $\sigma > 40 \text{ km s}^{-1}$ is $28\% \pm 8\%$ (uncertainties are given for the 90% confidence limit).

As expected, the detection fraction increases as we increase our sensitivity (i.e., lower the value of L_{det}), but does so similarly for the low and high velocity dispersion regimes.

4.3. Detection rate versus tidal encounter rate

We also look at the X-ray detection rate versus the tidal capture (TC) rates determined by Stone et al. (2017). The tidal capture rate \dot{N}_{TC} is given by equation 14 in Stone et al. (2017) and depends on the mass of the

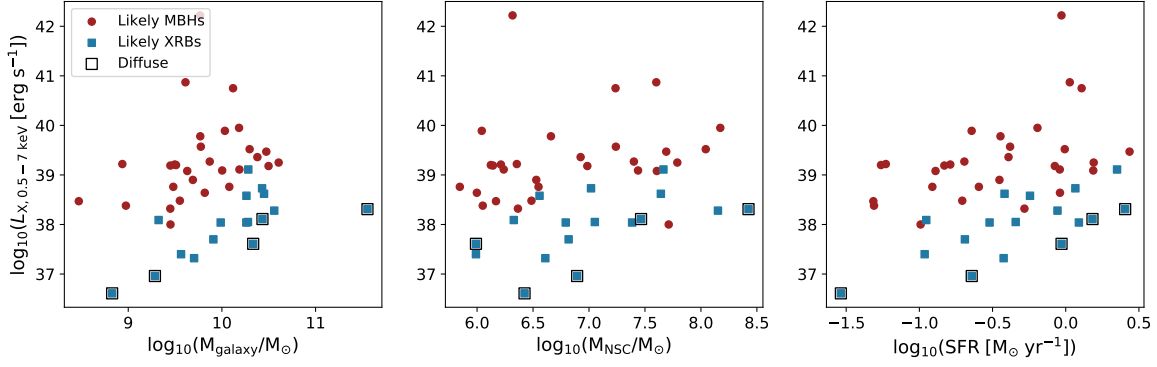


Figure 3. X-ray luminosity versus galaxy properties for X-ray detected galaxies that are likely massive BHs (red circles), and likely XRBs (blue squares). From left to right, we show galaxy stellar mass, NSC stellar mass, and galaxy star formation rate. At a given X-ray luminosity, the likely XRBs are in more massive galaxies/NSCs and have higher star formation rates. We also emphasize the galaxies with diffuse X-ray emission. These are all likely XRB systems and have some of the lowest detected X-ray luminosities.

Object	$M_{*,\text{galaxy}}$ [M_{\odot}]	SFR [$M_{\odot} \text{ yr}^{-1}$]	$L_{\text{XRBs},0.5-8\text{keV}}$ [$\log_{10}(\text{erg s}^{-1})$]	$L_{\text{source},0.5-8\text{keV}}$ [$\log_{10}(\text{erg s}^{-1})$]	$L_{\text{source}} / L_{\text{XRBs}}$
ESO138-G010	1.82E+10	0.3018	38.35	38.11	0.58
IC0396	4.23E+09	0.1290	38.18	39.15	9.33
M074	1.90E+10	0.4551	38.46	38.12	0.46
M108	2.16E+10	0.9364	38.64	37.68	0.11
NGC0247	2.82E+09	0.1482	36.79	39.26	296.59
NGC1042	2.11E+09	0.1115	37.90	38.16	1.84
NGC1058	2.83E+09	0.1020	37.63	38.07	2.74
NGC1073	4.90E+09	0.3525	38.05	38.97	8.34
NGC1385	5.85E+09	0.9353	38.69	42.29	3981.04
NGC1493	3.02E+09	0.2550	37.97	38.82	7.23
NGC1559	5.88E+09	0.3583	38.16	39.85	49.28
NGC1566	1.52E+10	0.6410	38.48	40.02	35.15
NGC2139	1.01E+10	1.5415	38.22	39.16	8.60
NGC2207	1.98E+10	0.9849	38.63	39.59	9.10
NGC2748	1.54E+10	0.9105	38.57	39.18	4.11
NGC2835	5.05E+09	0.3765	37.93	37.39	0.29
...

Table 3. X-ray binary contamination assessment. Column 4 gives the expected 0.5-8 keV luminosity from XRBs following the scalings derived in [Lehmer et al. \(2019\)](#). Column 5 gives the 0.5-8 keV luminosity of the detected X-ray source. Column 6 gives the ratio of the source luminosity to the expected XRB luminosity. The complete table will be available in the online version of the paper.

initial stellar-mass black hole, the velocity dispersion, central cluster density, and average mass and radius of the cluster stars. Some of the NSCs in our sample have only lower limits on the TC rate due to the discrete concentration values used in fitting the light profiles of the NSCs (objects with “Core Resolve” = 0 in Table 1). We exclude these from computations of the detection rate since we cannot say conclusively whether they are unstable to runaway TC over a Hubble time. We also note that the TC rates are uncertain by \sim one order of mag-

nitude for this reason. We refer the reader to Section 6.1 of [Stone et al. \(2017\)](#) for a detailed discussion of these uncertainties.

In Figure 9, we plot the X-ray detection fraction versus L_{det} for NSCs with TC rates above and below $\dot{N}_{\text{TC}} = 10^{-8} \text{ yr}^{-1}$. NSCs with TC rates $\dot{N}_{\text{TC}} > 10^{-8} \text{ yr}^{-1}$ should be unstable to runaway growth of a stellar-mass BH through TC. While the fractions are higher for the $\dot{N}_{\text{TC}} > 10^{-8} \text{ yr}^{-1}$ sample, the uncertainties are larger due to the smaller number of objects in the sample. The

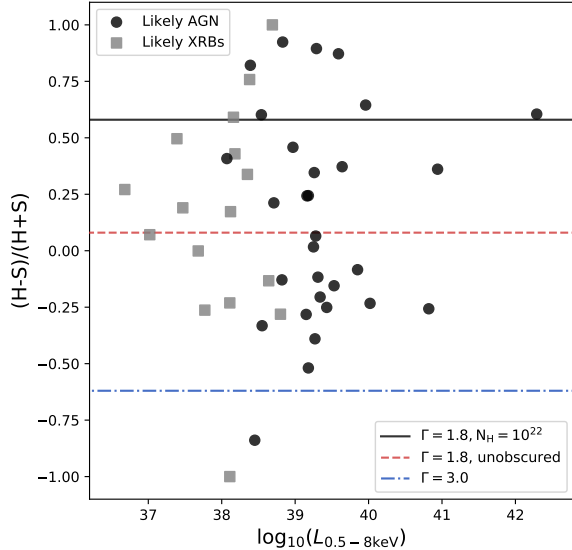


Figure 4. Hardness ratio versus 0.5-8 keV X-ray luminosity. H is the flux in the 2-7 keV band, and S is the flux in the 0.5-2 keV band. We use WebPIMMs to compute hardness ratios for sources with various power law indices. A power law index of $\Gamma = 1.8$ is typical of AGN; we show the hardness ratios for this value for an obscured and unobscured source. A power law index of $\Gamma = 3$ reflects a softer X-ray spectrum consistent with high Eddington fraction X-ray binaries (Yang et al. 2015).

two groups are consistent with one another within the 90% confidence intervals. In order to confirm whether the X-ray detection fractions are truly higher amongst NSCs with $\dot{N}_{\text{TC}} > 10^{-8} \text{ yr}^{-1}$, we will need to obtain better constrained measurements of \dot{N}_{TC} for a greater number of NSCs.

5. DISCUSSION

5.1. BH formation in NSCs

Our analysis finds that NSCs with velocity dispersions higher than 40 km s^{-1} are X-ray detected at roughly twice the rate of NSCs below that threshold. This is consistent with theories (Miller & Davies 2012; Stone et al. 2017) that suggest NSCs with high velocity dispersions can form and grow massive BHs.

This is not the only possible interpretation of our results. One alternative scenario is that the NSCs with higher velocity dispersions had pre-existing massive BHs and the NSC formed around the BH. One implication of this scenario is that these NSCs have higher velocity dispersions due to the presence of the BH. To further explore this scenario, we turn to results from Antonini (2013), which models the formation of NSCs through star cluster inspiral in galaxies with/without a

pre-existing massive BH. They find that if a massive BH is already present, the resulting NSC has a lower density than would form in a galaxy without a massive BH. In the presence of a pre-existing BH, the radius of the NSC is set by the tidal field of the BH. This could explain why NSCs are not typically found in galaxies with stellar masses greater than $\sim 10^{10} M_{\odot}$; the tidal field of a sufficiently large BH will prevent a NSC from forming³.

If the high- σ , X-ray detected NSCs formed around pre-existing BHs, they should have systematically lower densities. In Figure 10 we plot the distributions of mean density for NSCs with and without X-ray detections. For those with X-ray detections, we divide the sample into NSCs with σ above and below the 40 km s^{-1} threshold. We find that the X-ray detected, high- σ NSCs tend towards *higher* densities, in contrast to expectations for collisionless NSC formation around a pre-existing BH. Interestingly, the X-ray detected NSCs with low σ – those that do not meet the theoretical requirements for forming a massive BH – skew towards lower densities. Their lower densities are consistent with this population having formed around pre-existing BHs rather than forming a BH later on.

Another interpretation for our findings is that high density/high velocity dispersion NSCs are more efficient at fueling massive BHs, leading to higher accretion rates and thus higher X-ray luminosities. Naiman et al. (2015) simulates massive BH growth in NSCs during galaxy mergers. They find that NSCs can enhance BH fueling in this scenario, provided that the NSC meets the condition of $\sigma_{\text{NSC}} > v^2 + c_s^2$, where v is the relative velocity of the NSC through the gas, and c_s is the sound speed. However, this pertains only to systems undergoing mergers; simulations of the impact of NSCs on BH fueling in non-merging systems are needed.

Results from dynamical studies of nearby nucleated galaxies lend support to the scenario in which massive BHs can form and grow in high velocity-dispersion systems. M33 is one of the most nearby, well studied nuclei; HST kinematics show a NSC velocity dispersion of 24 km s^{-1} and no detected BH (at least to an upper limit of $1500 M_{\odot}$; Gebhardt et al. 2001; Merritt et al. 2001). Nguyen et al. (2018) carries out dynamical modeling of the nuclear star clusters in M32 (see also Seth 2010), NGC 205, NGC 5102, and NGC 5206. The three clusters that have velocity dispersions $> 40 \text{ km s}^{-1}$ – M32, NGC 5102, and NGC 5206 – are those that are

³ Other factors, such as the increasingly long dynamical friction inspiral time (Antonini 2013) and core scouring in multiple mergers (Thomas et al. 2014), also likely play a role in suppressing high-mass NSC formation.

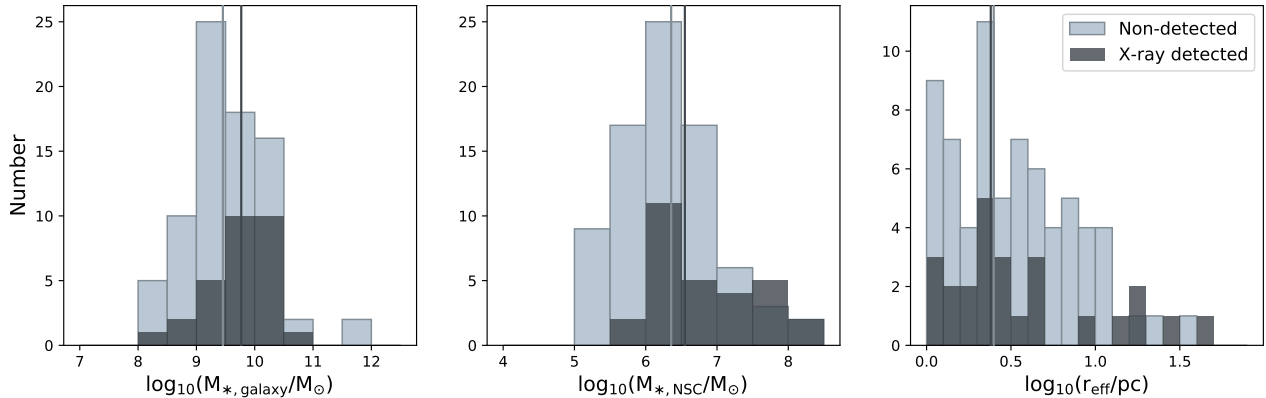


Figure 5. Properties of galaxies with and without X-ray detected NSCs. From left to right, we show galaxy stellar mass, NSC stellar mass, and NSC effective radius. The solid lines show the median values of each distribution.

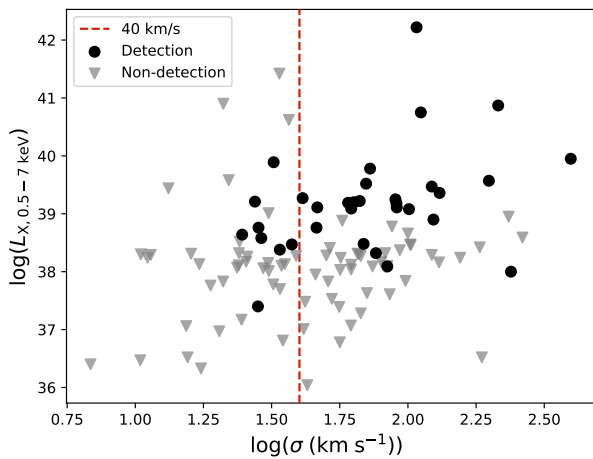


Figure 6. X-ray luminosity (0.5-7 keV) versus NSC 1-D velocity dispersion. Detections are shown as black circles, and upper limits are represented by gray triangles. The vertical dashed red line marks the 40 km s^{-1} threshold.

found to have evidence for central black holes. Nearby galaxies with X-ray detections presented here would be good targets for follow-up with high-resolution dynamical modeling.

These results also have important implications for our understanding of massive BH formation. If NSCs do facilitate the formation of massive BHs at relatively low redshift, this complicates efforts to use the present-day occupation fraction to constrain models of BH formation (see [Greene et al. 2020](#)). If massive BH seeds form only at high-redshift, the low-mass end of the occupation fraction is expected to be sensitive to high-redshift BH seed formation models. However, this effect could be washed out if NSCs (which reside in low-mass galaxies) form massive BHs at later epochs.

5.2. BH growth in low-mass galaxies

The most massive BHs are expected to be assembled by $z \sim 2$, with progressively lower mass BHs undergoing more of their growth at lower redshifts. This is known as “downsizing” in BH accretion ([Marconi et al. 2004](#); [Di Matteo et al. 2008](#)). In this section, we carry out a simple analysis to explore possible growth histories for the accreting BHs in the sample of nucleated galaxies presented here⁴.

In order to estimate the mass accreted over time, we assume the current 2-10 keV X-ray luminosity for each galaxy is representative and use it as an average X-ray luminosity for that BH over the last 10 Gyr. We assume a bolometric correction of 10 ([Marconi et al. 2004](#)) and a radiative efficiency of 10%. Using this analysis, we find accreted masses spanning a large range ($\sim 10 - 10^6 M_\odot$), with a mean accreted mass of $\sim 10^3 M_\odot$. The mean value is several orders of magnitude below the saturation mass, an order-of-magnitude estimate for BHs grown primarily through tidal capture and/or tidal disruption in NSCs ([Stone et al. 2017](#)). In [Figure 11](#), we show the estimated accreted mass versus the saturation mass for each of the X-ray detected systems.

This suggests that – if the current X-ray luminosities can generally be used to compute an average mass accretion rate – these BHs have not grown much through gas accretion. There are several ways to interpret this result. One possibility is that these BHs were more active in the past and underwent most of their growth at higher redshift. Given the general trend of downsizing in BH accretion, this seems unlikely. Another possibility is that

⁴ We note that [Georgiev & Böker \(2014\)](#) do exclude bright AGN from their initial sample of late-type galaxies based on their AGN class indicator in HyperLeda ([Paturel et al. 2003](#)). This primarily would have removed bright AGN in massive galaxies unlikely to have NSCs. Indeed, NGC 4395 – one of the brightest and well-known low-mass AGN – is still part of the sample.

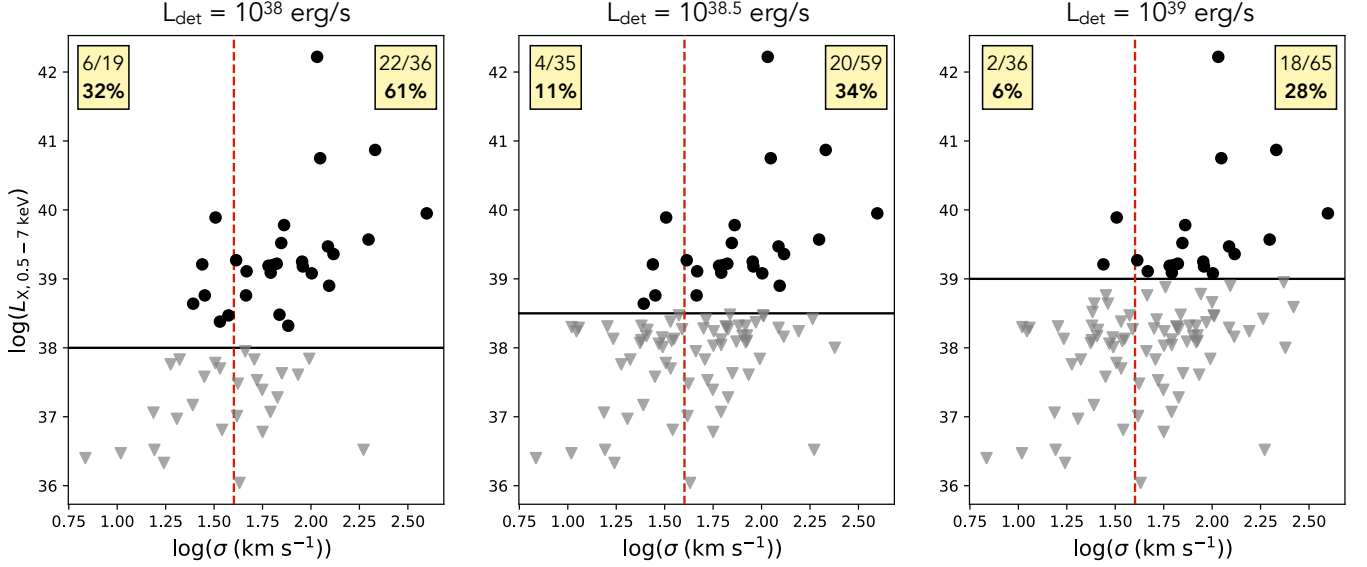


Figure 7. Same as Figure 6, but with different imposed detection limits, L_{det} . The horizontal black solid line shows L_{det} for each panel. Any X-ray detection below that limit is treated as an upper limit. We compute the detection fraction for NSCs with 1-D velocity dispersions above and below 40 km s^{-1} for each value of L_{det} . The detection fractions for each are shown at the top of each panel. The detection fractions for NSCs in the high velocity dispersion regime are consistently and significantly higher. We note that galaxies with X-ray emission likely to be due to X-ray binaries are also treated as non-detections, since they do not have X-ray detections consistent with the presence of a massive BH.

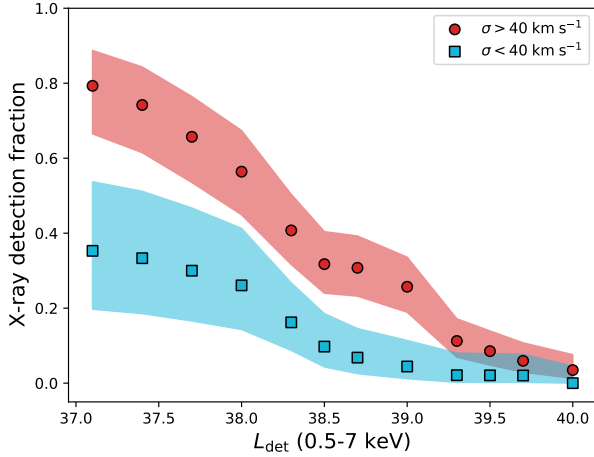


Figure 8. X-ray detection fraction versus L_{det} for NSCs with velocity dispersions above (red circles) and below (blue squares) 40 km s^{-1} . This is the nominal threshold above which NSCs are unstable to core collapse and will form a massive BH. The shaded region reflects the 90% confidence limits (Gehrels 1986).

the bolometric correction and/or radiative efficiency are higher for low-mass AGN. However, the accretion properties would have to be substantially different to make up for the several orders of magnitude difference between the estimated accreted mass and saturation mass. A third possibility is that BHs in low-mass galaxies grow

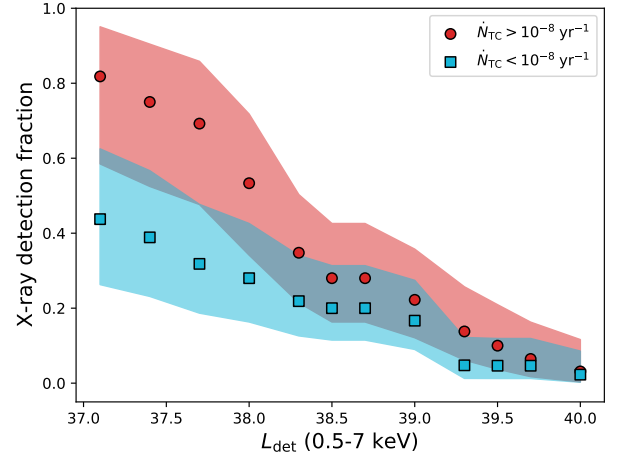


Figure 9. X-ray detection fraction versus L_{det} for NSCs with velocity dispersions above (red circles) and below (blue squares) $\dot{N}_{\text{TC}} = 10^{-8} \text{ yr}^{-1}$. This is the nominal threshold above which a stellar-mass BH in a NSC is unstable to growth through the tidal capture runaway (Stone et al. 2017). The shaded region reflects the 90% confidence limits (Gehrels 1986).

primarily through intermittent phases of short, highly super-Eddington accretion due to tidal capture and/or tidal disruption events. While there remain open questions surrounding the fraction of mass accreted in both tidal captures (Generozov et al. 2018) and in tidal dis-

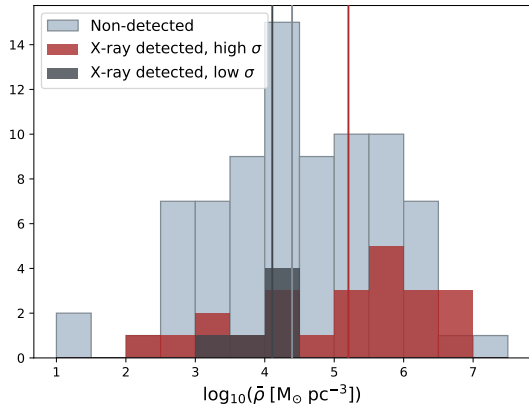


Figure 10. Mean density distributions for NSCs with/without X-ray detections. The mean density is defined as $\bar{\rho} = 3M_{\text{tot}}/(4\pi r_h^3)$. The sample of non-detected NSCs is shown in light gray. X-ray detected NSCs with $\sigma > 40 \text{ km s}^{-1}$ are shown in red. X-ray detected NSCs with $\sigma < 40 \text{ km s}^{-1}$ are shown in dark gray. The low- σ X-ray detected NSCs have on average lower densities than their high- σ counterparts.

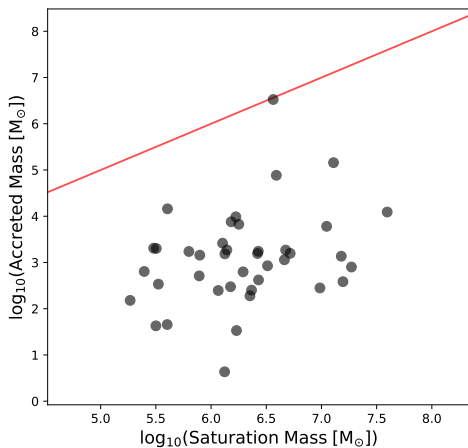


Figure 11. Accreted mass versus saturation mass for each X-ray detected galaxy. The accreted mass is estimated by assuming the present X-ray luminosity can be treated as an average over the last 10 Gyr (see Section 5.2). The saturation mass reflects the mass that a BH in a NSC will grow to through tidal capture and/or tidal disruption processes (equation 37 in Stone et al. 2017). The red line reflects a saturation mass equal to the accreted mass.

ruption events (Metzger & Stone 2016; Bonnerot & Lu 2020), we consider this the most likely scenario. This is consistent with recent work demonstrating that the duty

cycles of TDE-powered AGN are consistent with the observed fractions of AGN in present-day dwarf galaxies (Zubovas 2019).

6. SUMMARY

We analyze *Chandra X-ray Observatory* imaging for 108 nearby galaxies with NSCs. Of these, 29 have X-ray emission that is likely to be due to an accreting massive BH. We then study the properties of NSCs with and without evidence for massive BHs. Our conclusions can be summarized as follows:

1. NSCs with mean velocity dispersions $> 40 \text{ km s}^{-1}$ are X-ray detected at roughly twice the rate of those below this threshold.
2. Tentatively, NSCs with TC rates high enough to form an intermediate-mass BH in less than a Hubble time are X-ray detected at a higher rate than those below this limit.
3. These results are consistent with a scenario in which sufficiently dense, high velocity dispersion NSCs can form an intermediate-mass BH through dynamical processes.
4. Better constraints on the active fraction as a function of velocity dispersion and TC rate could be obtained by improved morphological modeling of the NSCs (i.e., finer sampling of the concentration parameters) and additional X-ray observations.

The authors thank Decker French for insightful comments which have improved this manuscript. We thank the anonymous referee for their careful reading of the manuscript and for their suggestions.

Support for this work was provided by the National Aeronautics and Space Administration through Chandra Award Number GO9-20102X issued by the Chandra X-ray Center, which is operated by the Smithsonian Astrophysical Observatory for and on behalf of the National Aeronautics Space Administration under contract NAS8-03060. The scientific results reported in this article are based on observations made by the Chandra X-ray Observatory through GO-20700424 and data obtained from the Chandra Data Archive. This research has made use of software provided by the Chandra X-ray Center (CXC) in the application packages CIAO, ChIPS, and Sherpa.

REFERENCES

Agarwal, M., & Milosavljević, M. 2011, *ApJ*, 729, 35, doi: 10.1088/0004-637X/729/1/35

Antonini, F. 2013, *ApJ*, 763, 62, doi: 10.1088/0004-637X/763/1/62

- Antonini, F., Capuzzo-Dolcetta, R., Mastrobuono-Battisti, A., & Merritt, D. 2012, *ApJ*, 750, 111, doi: [10.1088/0004-637X/750/2/111](https://doi.org/10.1088/0004-637X/750/2/111)
- Antonini, F., Gieles, M., & Gualandris, A. 2019, *MNRAS*, 486, 5008, doi: [10.1093/mnras/stz1149](https://doi.org/10.1093/mnras/stz1149)
- Begelman, M. C., Volonteri, M., & Rees, M. J. 2006, *MNRAS*, 370, 289, doi: [10.1111/j.1365-2966.2006.10467.x](https://doi.org/10.1111/j.1365-2966.2006.10467.x)
- Birchall, K. L., Watson, M. G., & Aird, J. 2020, arXiv e-prints, arXiv:2001.03135. <https://arxiv.org/abs/2001.03135>
- Böker, T., Laine, S., van der Marel, R. P., et al. 2002, *AJ*, 123, 1389, doi: [10.1086/339025](https://doi.org/10.1086/339025)
- Böker, T., Sarzi, M., McLaughlin, D. E., et al. 2004, *AJ*, 127, 105, doi: [10.1086/380231](https://doi.org/10.1086/380231)
- Bonnerot, C., & Lu, W. 2020, *MNRAS*, 495, 1374, doi: [10.1093/mnras/staa1246](https://doi.org/10.1093/mnras/staa1246)
- Capuzzo-Dolcetta, R., & Miocchi, P. 2008, *ApJ*, 681, 1136, doi: [10.1086/588017](https://doi.org/10.1086/588017)
- Carson, D. J., Barth, A. J., Seth, A. C., et al. 2015, *AJ*, 149, 170, doi: [10.1088/0004-6256/149/5/170](https://doi.org/10.1088/0004-6256/149/5/170)
- Clark, G. W. 1975, *ApJL*, 199, L143, doi: [10.1086/181869](https://doi.org/10.1086/181869)
- Côté, P., Piatek, S., Ferrarese, L., et al. 2006, *ApJS*, 165, 57, doi: [10.1086/504042](https://doi.org/10.1086/504042)
- Di Matteo, T., Colberg, J., Springel, V., Hernquist, L., & Sijacki, D. 2008, *ApJ*, 676, 33, doi: [10.1086/524921](https://doi.org/10.1086/524921)
- Ebisuzaki, T., Makino, J., & Okumura, S. K. 1991, *Nature*, 354, 212, doi: [10.1038/354212a0](https://doi.org/10.1038/354212a0)
- Fabian, A. C., Pringle, J. E., & Rees, M. J. 1975, *MNRAS*, 172, 15, doi: [10.1093/mnras/172.1.15P](https://doi.org/10.1093/mnras/172.1.15P)
- Fahrion, K., Lyubenova, M., van de Ven, G., et al. 2021, arXiv e-prints, arXiv:2104.06412. <https://arxiv.org/abs/2104.06412>
- Ferrarese, L., Côté, P., Jordán, A., et al. 2006a, *ApJ*, 164, 334
- Ferrarese, L., Côté, P., Bonta, E. D., et al. 2006b, *ApJ*, 644, L21
- Foord, A., Gallo, E., Hodges-Kluck, E., et al. 2017, *ApJ*, 841, 51, doi: [10.3847/1538-4357/aa6d63](https://doi.org/10.3847/1538-4357/aa6d63)
- Fragione, G., Kocsis, B., Rasio, F. A., & Silk, J. 2021, arXiv e-prints, arXiv:2107.04639. <https://arxiv.org/abs/2107.04639>
- Fragione, G., & Silk, J. 2020, *MNRAS*, 498, 4591, doi: [10.1093/mnras/staa2629](https://doi.org/10.1093/mnras/staa2629)
- Gebhardt, K., Lauer, T. R., Kormendy, J., et al. 2001, *AJ*, 122, 2469, doi: [10.1086/323481](https://doi.org/10.1086/323481)
- Gehrels, N. 1986, *ApJ*, 303, 336, doi: [10.1086/164079](https://doi.org/10.1086/164079)
- Generozov, A., Stone, N. C., Metzger, B. D., & Ostriker, J. P. 2018, *MNRAS*, 478, 4030, doi: [10.1093/mnras/sty1262](https://doi.org/10.1093/mnras/sty1262)
- Georgiev, I. Y., & Böker, T. 2014, *MNRAS*, 441, 3570, doi: [10.1093/mnras/stu797](https://doi.org/10.1093/mnras/stu797)
- Georgiev, I. Y., Böker, T., Leigh, N., Lützgendorf, N., & Neumayer, N. 2016, *MNRAS*, 457, 2122, doi: [10.1093/mnras/stw093](https://doi.org/10.1093/mnras/stw093)
- Gilfanov, M. 2004, *MNRAS*, 349, 146
- Gnedin, O. Y., Ostriker, J. P., & Tremaine, S. 2014, *ApJ*, 785, 71, doi: [10.1088/0004-637X/785/1/71](https://doi.org/10.1088/0004-637X/785/1/71)
- González, E., Kremer, K., Chatterjee, S., et al. 2021, *ApJL*, 908, L29, doi: [10.3847/2041-8213/abdf5b](https://doi.org/10.3847/2041-8213/abdf5b)
- Greene, J. E., Strader, J., & Ho, L. C. 2020, *ARA&A*, 58, 257, doi: [10.1146/annurev-astro-032620-021835](https://doi.org/10.1146/annurev-astro-032620-021835)
- Grimm, H.-J., Gilfanov, M., & Sunyaev, R. 2003, *MNRAS*, 339, 793, doi: [10.1046/j.1365-8711.2003.06224.x](https://doi.org/10.1046/j.1365-8711.2003.06224.x)
- Gürkan, M. A., Freitag, M., & Rasio, F. A. 2004, *ApJ*, 604, 632, doi: [10.1086/381968](https://doi.org/10.1086/381968)
- Hailey, C. J., Mori, K., Bauer, F. E., et al. 2018, *Nature*, 556, 70, doi: [10.1038/nature25029](https://doi.org/10.1038/nature25029)
- Haiman, Z., & Loeb, A. 2001, *ApJ*, 552, 459, doi: [10.1086/320586](https://doi.org/10.1086/320586)
- Hannah, C. H., Seth, A. C., Nguyen, D. D., et al. 2021, arXiv e-prints, arXiv:2109.12251. <https://arxiv.org/abs/2109.12251>
- Hoyer, N., Neumayer, N., Georgiev, I. Y., Seth, A. C., & Greene, J. E. 2021, arXiv e-prints, arXiv:2107.05313. <https://arxiv.org/abs/2107.05313>
- Inayoshi, K., Visbal, E., & Haiman, Z. 2020, *ARA&A*, 58, 27, doi: [10.1146/annurev-astro-120419-014455](https://doi.org/10.1146/annurev-astro-120419-014455)
- Ivanova, N., Heinke, C. O., Rasio, F. A., Belczynski, K., & Fregeau, J. M. 2008, *MNRAS*, 386, 553, doi: [10.1111/j.1365-2966.2008.13064.x](https://doi.org/10.1111/j.1365-2966.2008.13064.x)
- Kennicutt, R. C., & Evans, N. J. 2012, *ARA&A*, 50, 531, doi: [10.1146/annurev-astro-081811-125610](https://doi.org/10.1146/annurev-astro-081811-125610)
- King, I. R. 1966, *AJ*, 71, 64, doi: [10.1086/109857](https://doi.org/10.1086/109857)
- Kormendy, J., & Ho, L. C. 2013, *ARA&A*, 51, 511, doi: [10.1146/annurev-astro-082708-101811](https://doi.org/10.1146/annurev-astro-082708-101811)
- Kremer, K., Spera, M., Becker, D., et al. 2020, *ApJ*, 903, 45, doi: [10.3847/1538-4357/abb945](https://doi.org/10.3847/1538-4357/abb945)
- Latif, M. A., Schleicher, D. R. G., Schmidt, W., & Niemeyer, J. C. 2013, *MNRAS*, 436, 2989, doi: [10.1093/mnras/stt1786](https://doi.org/10.1093/mnras/stt1786)
- Lee, H. M., & Ostriker, J. P. 1986, *ApJ*, 310, 176, doi: [10.1086/164674](https://doi.org/10.1086/164674)
- Lee, N., Gallo, E., Hodges-Kluck, E., et al. 2019, *ApJ*, 874, 77, doi: [10.3847/1538-4357/ab05cd](https://doi.org/10.3847/1538-4357/ab05cd)
- Lehmer, B. D., Eufrazio, R. T., Tzanavaris, P., et al. 2019, *ApJS*, 243, 3, doi: [10.3847/1538-4365/ab22a8](https://doi.org/10.3847/1538-4365/ab22a8)
- Leigh, N., Böker, T., & Knigge, C. 2012, *MNRAS*, 424, 2130, doi: [10.1111/j.1365-2966.2012.21365.x](https://doi.org/10.1111/j.1365-2966.2012.21365.x)

- Loeb, A., & Rasio, F. A. 1994, *ApJ*, 432, 52, doi: [10.1086/174548](https://doi.org/10.1086/174548)
- Lotz, J. M., Telford, R., Ferguson, H. C., et al. 2001, *ApJ*, 552, 572, doi: [10.1086/320545](https://doi.org/10.1086/320545)
- Madau, P., & Rees, M. J. 2001, *ApJL*, 551, L27, doi: [10.1086/319848](https://doi.org/10.1086/319848)
- Marconi, A., Risaliti, G., Gilli, R., et al. 2004, *MNRAS*, 351, 169, doi: [10.1111/j.1365-2966.2004.07765.x](https://doi.org/10.1111/j.1365-2966.2004.07765.x)
- Martin, D. C., Fanson, J., Schiminovich, D., et al. 2005, *ApJL*, 619, L1, doi: [10.1086/426387](https://doi.org/10.1086/426387)
- Mayer, L., Kazantzidis, S., Escala, A., & Callegari, S. 2010, *Nature*, 466, 1082, doi: [10.1038/nature09294](https://doi.org/10.1038/nature09294)
- Merritt, D., Ferrarese, L., & Joseph, C. L. 2001, *Science*, 293, 1116, doi: [10.1126/science.1063896](https://doi.org/10.1126/science.1063896)
- Metzger, B. D., & Stone, N. C. 2016, *MNRAS*, 461, 948, doi: [10.1093/mnras/stw1394](https://doi.org/10.1093/mnras/stw1394)
- Miller, M. C., & Davies, M. B. 2012, *ApJ*, 755, 81, doi: [10.1088/0004-637X/755/1/81](https://doi.org/10.1088/0004-637X/755/1/81)
- Mineo, S., Gilfanov, M., & Sunyaev, R. 2012, *MNRAS*, 419, 2095, doi: [10.1111/j.1365-2966.2011.19862.x](https://doi.org/10.1111/j.1365-2966.2011.19862.x)
- Muno, M. P., Pfahl, E., Baganoff, F. K., et al. 2005, *ApJL*, 622, L113, doi: [10.1086/429721](https://doi.org/10.1086/429721)
- Naiman, J. P., Ramirez-Ruiz, E., Debuhr, J., & Ma, C.-P. 2015, *ApJ*, 803, 81, doi: [10.1088/0004-637X/803/2/81](https://doi.org/10.1088/0004-637X/803/2/81)
- Natarajan, P. 2021, *MNRAS*, 501, 1413, doi: [10.1093/mnras/staa3724](https://doi.org/10.1093/mnras/staa3724)
- Neumayer, N., Seth, A., & Böker, T. 2020, *A&A Rv*, 28, 4, doi: [10.1007/s00159-020-00125-0](https://doi.org/10.1007/s00159-020-00125-0)
- Nguyen, D. D., Seth, A. C., Neumayer, N., et al. 2018, *ApJ*, 858, 118, doi: [10.3847/1538-4357/aabe28](https://doi.org/10.3847/1538-4357/aabe28)
- Nguyen, D. D., Bureau, M., Thater, S., et al. 2021, arXiv e-prints, arXiv:2110.08476. <https://arxiv.org/abs/2110.08476>
- Paturel, G., Petit, C., Prugniel, P., et al. 2003, *A&A*, 412, 45, doi: [10.1051/0004-6361:20031411](https://doi.org/10.1051/0004-6361:20031411)
- Portegies Zwart, S. F., Baumgardt, H., Hut, P., Makino, J., & McMillan, S. L. W. 2004, *Nature*, 428, 724, doi: [10.1038/nature02448](https://doi.org/10.1038/nature02448)
- Portegies Zwart, S. F., & McMillan, S. L. W. 2002, *ApJ*, 576, 899, doi: [10.1086/341798](https://doi.org/10.1086/341798)
- Pouliasis, E., Georgantopoulos, I., Bonanos, A. Z., et al. 2019, *MNRAS*, 487, 4285, doi: [10.1093/mnras/stz1483](https://doi.org/10.1093/mnras/stz1483)
- Quinlan, G. D. 1996, *NewA*, 1, 35, doi: [10.1016/S1384-1076\(96\)00003-6](https://doi.org/10.1016/S1384-1076(96)00003-6)
- Sánchez-Janssen, R., Côté, P., Ferrarese, L., et al. 2019, *ApJ*, 878, 18, doi: [10.3847/1538-4357/aaf4fd](https://doi.org/10.3847/1538-4357/aaf4fd)
- Schödel, R., Merritt, D., & Eckart, A. 2009, *A&A*, 502, 91, doi: [10.1051/0004-6361/200810922](https://doi.org/10.1051/0004-6361/200810922)
- Seth, A., Agüeros, M., Lee, D., & Basu-Zych, A. 2008, *ApJ*, 678, 116, doi: [10.1086/528955](https://doi.org/10.1086/528955)
- Seth, A. C. 2010, *ApJ*, 725, 670, doi: [10.1088/0004-637X/725/1/670](https://doi.org/10.1088/0004-637X/725/1/670)
- Seth, A. C., Dalcanton, J. J., Hodge, P. W., & Debattista, V. P. 2006, *AJ*, 132, 2539, doi: [10.1086/508994](https://doi.org/10.1086/508994)
- Sivakoff, G., Jordán, A., Sarazin, C., et al. 2007, *ApJ*, 660, 1246
- Stone, N. C., Küpper, A. H. W., & Ostriker, J. P. 2017, *MNRAS*, 467, 4180, doi: [10.1093/mnras/stx097](https://doi.org/10.1093/mnras/stx097)
- Thomas, J., Saglia, R. P., Bender, R., Erwin, P., & Fabricius, M. 2014, *ApJ*, 782, 39, doi: [10.1088/0004-637X/782/1/39](https://doi.org/10.1088/0004-637X/782/1/39)
- Tremaine, S. D., Ostriker, J. P., & Spitzer, Jr., L. 1975, *ApJ*, 196, 407, doi: [10.1086/153422](https://doi.org/10.1086/153422)
- Turner, M., Cote, P., Ferrarese, L., et al. 2012, *ApJS*
- Volonteri, M. 2010, *A&A Rv*, 18, 279, doi: [10.1007/s00159-010-0029-x](https://doi.org/10.1007/s00159-010-0029-x)
- Walcher, C. J., Böker, T., Charlot, S., et al. 2006, *ApJ*, 649, 692, doi: [10.1086/505166](https://doi.org/10.1086/505166)
- Whalen, D. J., & Fryer, C. L. 2012, *ApJL*, 756, L19, doi: [10.1088/2041-8205/756/1/L19](https://doi.org/10.1088/2041-8205/756/1/L19)
- Wright, E. L., Eisenhardt, P. R. M., Mainzer, A. K., et al. 2010, *AJ*, 140, 1868, doi: [10.1088/0004-6256/140/6/1868](https://doi.org/10.1088/0004-6256/140/6/1868)
- Yang, Q.-X., Xie, F.-G., Yuan, F., et al. 2015, *MNRAS*, 447, 1692, doi: [10.1093/mnras/stu2571](https://doi.org/10.1093/mnras/stu2571)
- Zubovas, K. 2019, *MNRAS*, 483, 1957, doi: [10.1093/mnras/sty3211](https://doi.org/10.1093/mnras/sty3211)